2nd Advanced Optical Metrology Compendium

Advanced Optical Metrology

Geoscience | Corrosion | Particles | Additive
Manufacturing: Metallurgy, Cut Analysis & Porosity

EVIDENT
OLYMPUS

WILEY

The latest eBook from Advanced Optical Metrology. Download for free.

This compendium includes a collection of optical metrology papers, a repository of teaching materials, and instructions on how to publish scientific achievements.

With the aim of improving communication between fundamental research and industrial applications in the field of optical metrology we have collected and organized existing information and made it more accessible and useful for researchers and practitioners.

EVIDENT
OLYMPUS

WILEY

Silica-Coated Gold Nanorod Supraparticles: A Tunable Platform for Surface Enhanced Raman Spectroscopy

Jessi E.S. van der Hoeven,* Harith Gurunarayanan, Maarten Bransen, D.A. Matthijs de Winter, Petra E. de Jongh, and Alfons van Blaaderen*

Plasmonic nanoparticle assemblies are promising functional materials for surface-enhanced Raman spectroscopy (SERS). Gold nanorod (AuNR) assemblies are of particular interest due to the large, shape-induced local field enhancement and the tunable surface plasmon resonance of the AuNRs. Designing the optimal assembly structure for SERS, however, is challenging and requires a delicate balance between the interparticle distance, porosity, and wetting of the assembly. Here, a new type of functional assemblies–called supraparticles–fabricated through the solvent-evaporation driven assembly of silica-coated gold nanorods into spherical ensembles, in which the plasmonic coupling and the mass transport is tuned through the thickness and porosity of the silica shells are introduced. Etching of the AuNRs allowed fine-tuning of the plasmonic response to the laser excitation wavelength. Using a correlative SERS-electron microscopy approach, it is shown that all supraparticles successfully amplified the Raman signal of the crystal violet probe molecules, and that the Raman signal strongly increased when decreasing the silica shell thickness from 35 to 3 nm, provided that the supraparticles have a sufficiently high porosity. The supraparticles introduced in this study present a novel class of materials for sensing, and open up a wide parameter space to optimize their performance.

1. Introduction

Nowadays surface-enhanced Raman spectroscopy (SERS) is used in the detection of trace amounts of molecules and applied

in many fields ranging from single-molecule spectroscopy[1] and catalysis,[2–4] to biomedicine,[1,5] forensic research[6] and even art history.[7] SERS relies on the use of plasmonic nanoparticles (NPs) which can strongly enhance the Raman signal of scattering molecules close to the plasmonic NP surface. The SERS performance is very sensitive to the plasmonic properties of the metal NPs. Small improvements in local field enhancements around the NP surface can induce a large increase in the Raman signal, as the latter scales with the field enhancement to the 4th power.[8–10] The SERS performance of a plasmonic nanoparticle can therefore be tuned via the particle size, shape, morphology, and metal composition.[11–14]

Rod-shaped particles are particularly promising candidates for sensing applications. Gold nanorods (AuNRs) exhibit superior plasmonic properties compared to spheres as they have enhanced and highly tunable plasmonic properties due to their longitudinal surface plasmon resonance in the visible and near-infrared.[15] By precisely tuning the aspect ratio of the AuNRs the longitudinal LSPR can be matched to the wavelength of the excitation source used in SERS, thereby further enhancing the Raman scattering.[16–18] Furthermore, by assembling these AuNRs in larger superstructures, the LSPRs of the individual AuNRs can (partially) be overlapped, which gives rise to plasmonic hotspots between the AuNRs.[19] The strength of the local field enhancement in these hotspots can be tuned via the interparticle spacing and the orientation of the AuNRs.[19–26]

There are several ways to create nanoparticle assemblies with plasmonic interparticle hotspots.[15] One can use bottom-up approaches using molecular linkers[8,15,21,27–29] or evaporation-driven self-assembly[15,24,28,30–35] for facile and scalable fabrication of nanoparticle assemblies, or use top-down methods such as focused-ion-beam and template-assisted methods to achieve SERS substrates with uniform hotspots.[36,37] The molecularly linked assemblies typically contain a small number of NPs, rendering accessible- but few plasmonic hotspots.[32] Templated directed methods on the other hand can yield nanometer- to micron-sized colloidal crystals containing tens to thousands of NPs.[30,32,34,35] The SERS performance of the larger assemblies becomes hampered by diffusion limitations due to the

J. E. S. van der Hoeven, H. Gurunarayanan, M. Bransen,
D.A. M. de Winter, A. van Blaaderen
Soft Condensed Matter
Debye Institute for Nanomaterials Science
Utrecht University
Utrecht, The Netherlands
E-mail: j.e.s.vanderhoeven@uu.nl; a.vanblaaderen@uu.nl
J. E. S. van der Hoeven, P. E. de Jongh
Materials Chemistry and Catalysis
Debye Institute for Nanomaterials Science
Utrecht University
Utrecht, The Netherlands

small interparticle distances between the AuNRs, low assembly porosity, and large diffusion distances. This makes that the probe molecules can only access outer particle layers, whereas a large number of hotspots is located in the interior of the AuNR assembly.[31,32] The molds used in template-assisted approaches restrict the range of assembly sizes and shapes that can be fabricated, and result in assemblies fixed in or on a substrate. More flexible, soft-templated assembly approaches to make intermediate assembly sizes (100–1000 nm), and assemblies dispersed in a liquid would be advantageous in achieving a large number of accessible interparticle hotspots, and facile deposition of the assemblies on various surfaces for local sensing applications. Lastly, sufficient uptake of the probe molecules into the assemblies requires good wetting of the liquid in which the probe molecules are dissolved on the assembly surfaces. Infiltrating the structure with mesoporous silica after the assembly process can increase the wetting of the analyte solution and porosity of the assembly, and therefore the SERS performance.[30] Altogether, this indicates that further improvement of plasmonic particle ensembles for sensing is possible if more precise tuning of the assembly's porosity, wetting, interparticle distances, and size becomes possible.

Here, we fabricate spherical assemblies – called supraparticles – via a soft-template, solvent evaporation-based method in which an aqueous dispersion of silica-coated gold nanorods ($Au@SiO_2$ NRs) was emulsified in a larger apolar oil phase. The size of the supraparticles was adjusted between 100 nm and 2 µm via the water droplet size. The mass-transport and plasmonic properties of the assemblies were controlled by tuning the thickness and porosity of the silica coating of the individual nanorods, and by adjusting the aspect ratio of the AuNR via oxidative etching prior to the assembly process. Using a correlative SERS-electron microscopy (SERS-EM) approach, the various assembly structures were related to their SERS properties.

2. Results

2.1. Designing the Gold Nanorod Building Blocks

The interparticle distance, plasmonic properties, and porosity of the supraparticles were controlled via the structure of the individual $Au@SiO_2$ building blocks. **Figure 1** illustrates the tunability in shell thickness, porosity, and Au-core size of the silica-coated AuNRs. Adjusting the shell-thickness is key in controlling the plasmonic coupling between the $Au@SiO_2$ NRs in the supraparticles, which is particularly important for interparticle distances below 10 nm.[38] The thickness of thin, microporous silica shells was successfully controlled in this size regime (Figure 1a), and set between 3 and 7 nm via the reaction temperature and/or the reaction time in the silica synthesis (Figure S1, Supporting Information, see Method Section for details).

Apart from the shell thickness, also the porosity of the shells can be tuned. The electron microscopy images in Figure 1b show AuNRs coated with non-porous (or depending on the conditions ultramicroporous[39–41]) Stöber silica shells, as well as AuNRs coated with mesoporous silica shells with a pore size of 2.5 nm[42] and mesoporous silica shells with enlarged 4–5 nm pores. The mesopores were created by growing the silica shells
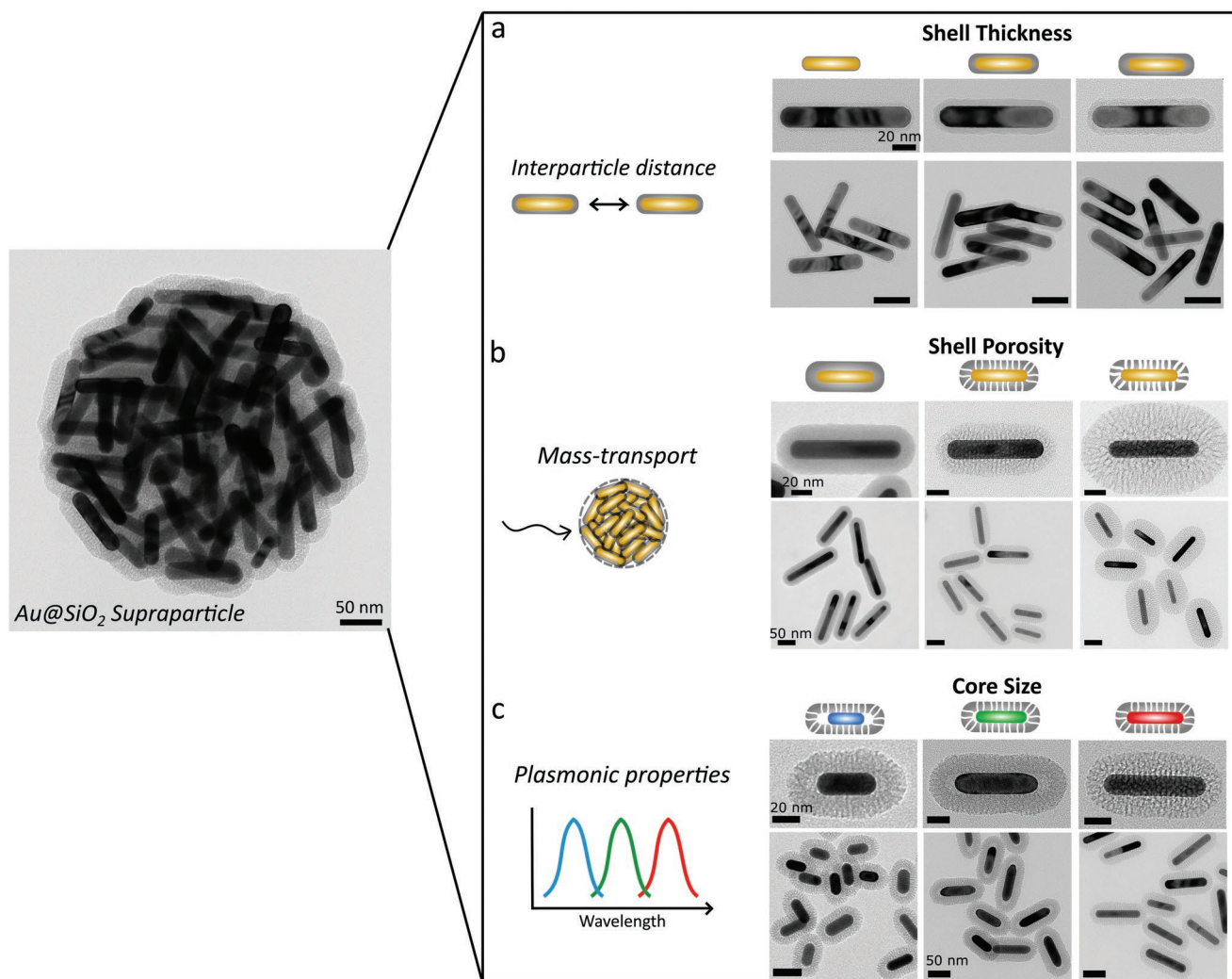
in the presence of hexadecyltrimethylammonium bromide (CTAB).[43] When the CTAB concentration is above the critical micelle concentration (≈1 mM in water), the positively charged CTAB micelles function as a template for the mesopore formation in the negatively charged silica coating. The resulting silica shells had mesopores with a diameter of 2.5 nm, and a Brunauer–Emmett–Teller surface area of 235 m^2 g^{-1} following from N_2-physisorption analysis.[42] Larger, 4–5 nm pores were created by adding a mixture of toluene and decane to swell the CTAB micelles, similar to the method described by Zhang et al. for the growth of mesoporous shells around iron oxide NPs.[44] Even larger pores can be achieved by further increasing the toluene-decane content.[44] Finally, also the core size of the AuNRs was tuned to match the LSPR of the AuNRs to the wavelength of laser light used in Raman spectroscopy experiments (Figure 1c). Oxidative etching in MeOH using H_2O_2 as an oxidant was used to selectively etch the AuNRs at their tips, thereby decreasing the aspect ratio (AR) of the rods and shifting the LSPR peak position from the near-infrared into the visible region of the spectrum (Figure S2, Supporting Information).[42]

The accessibility of AuNRs with the microporous, mesoporous, and non-porous silica shells was verified using pyridine as analyte molecules in Raman spectroscopy.[45] For the mesoporous silica-coated AuNR the CTAB-template was first removed from the mesopores by washing with an acidified ethanol solution (0.10 M HCl).[46] The Raman spectra in Figure S3, Supporting Information confirm that the Au surface of all $Au@SiO_2$ NRs except the non-porous, Stöber silica-coated AuNRs were accessible for pyridine and that no Raman signal from CTAB was detected (Figure S4, Supporting Information), indicating successful removal of the CTAB template.

2.2. Self-assembly of silica-coated gold nanorods into supraparticles

The silica-coated AuNRs were assembled into spherical supraparticles via a solvent evaporation approach (**Figure 2**).[47,48] Our methodology was based on that of Nijs et al.,[47,48] but now uses a water-in-oil instead of an oil-in-water emulsion. The oil-in-water method is not suitable for preparing $Au@SiO_2$ NR supraparticles for sensing applications as the $Au@SiO_2$ NRs need to be functionalized with a hydrophobic coating for dispersion in the oil phase, which makes the resulting structures inaccessible for polar analyte solutions due to low wetting. Therefore, a water-in-oil emulsion was used in preparing the $Au@SiO_2$ NRs supraparticles for this study, where the oil phase consisted of hexadecane with 1.0 wt% SPAN80 as a surfactant to stabilize the water droplets.

In Figure 2a the assembly process is schematically depicted. First, an aqueous dispersion of the $Au@SiO_2$ NRs (≈0.2 vol% in H_2O) was emulsified with a continuous oil phase. Subsequent drying of the water phase caused shrinkage of the water droplets and led to the formation of spherical supraparticles with close-packed $Au@SiO_2$ NRs. In Figure 2b,c electron microscopy images of $Au@SiO_2$ NRs ($L_{Au} = 95 \pm 8$ nm, $D_{Au} = 17 \pm 2$ nm, $d_{shell} = 18$ nm, and $d_{pore} = 2.5$ nm) before and after self-assembly are shown. Electron tomography of the supraparticles showed that the $Au@SiO_2$

ADVANCED
SCIENCE NEWS
www.advancedsciencenews.com

ADVANCED
FUNCTIONAL
**MATERIALS**
www.afm-journal.de

Figure 1. Silica-coated AuNR supraparticles as a tunable platform for sensing: the interparticle distance, mass- and heat-transport and plasmonic properties can all be tuned via the properties of the individual Au@SiO$_2$ NR building blocks. a) 3 nm (left), 5 nm (middle), and 7 nm (right) thick microporous silica shells on AuNRs. b) Non-porous Stöber silica-coated AuNRs with a shell thickness of 16 nm (left), mesoporous 18 nm thick silica-coated AuNRs with pores of about 2.5 nm (middle), and mesoporous silica-coated AuNRs with 4–5 nm wide pores and a shell thickness of 35 nm (right). c) Mesoporous silica-coated AuNRs with a core size of 43 ± 8 × 20 ± 2 nm (left), 66 ± 12 × 17 ± 2 (middle) and 95 ± 8 × 17 ± 2 nm (right). See the Method section for synthesis details.

NRs were randomly oriented in the spherical clusters (Movie S1, Supporting Information), which is due to their relatively low aspect ratio (AR_{Au} = 5.5, $AR_{Au+SiO2}$ ≈2.5).[48] The average size of the supraparticles was set via the size of the water droplets in combination with the volume fraction of the rods inside the initial water phase, which was varied by emulsifying the water and oil at different mixing speeds (keeping the volume fraction of the rods the same at ≈0.2 vol%). The final dried supraparticles prepared from emulsions mixed at 6000, 10 000, and 18 000 rpm had an average size of 380, 480, and 960 nm, respectively (Figure 2e). The size distribution of the supraparticles depends on the size distribution of the emulsion droplets, which is rather broad when using simple mixing approaches for the emulsification (Figure S5, Supporting Information). The emulsification was carried out on a 5 mL scale, but it can be scaled up to larger emulsion volumes, containing higher rod concentrations to further

increase the supraparticle yield. The visible-near infrared (VIS-NIR) spectra in Figure 2d reveal that although AuNRs were coated with a relatively thick (18 nm) silica shell, some coupling of the AuNR plasmons occurred, leading to a red-shift of ≈100 nm and broadening of the LSPR for the supraparticles compared to the non-assembled Au@SiO$_2$ NR.

The generality of our assembly method is demonstrated by the set of supraparticles with distinct porosities, interparticle distances, and core sizes displayed in **Figure 3**. By assembling Au@SiO$_2$ NRs with increasing shell thickness (3, 18, and 35 nm), supraparticles with larger interparticle distances between the AuNRs, and hence adjustable LSPR coupling were synthesized (Figure 3a–c). The low magnification EM images show that for all Au@SiO$_2$ NRs spherical supraparticles of various sizes were obtained, and also some aggregates in the case of the 3 nm thin silica coating (Figure 3a). The volume fraction of Au@SiO$_2$ NRs in the emulsion droplets calculated
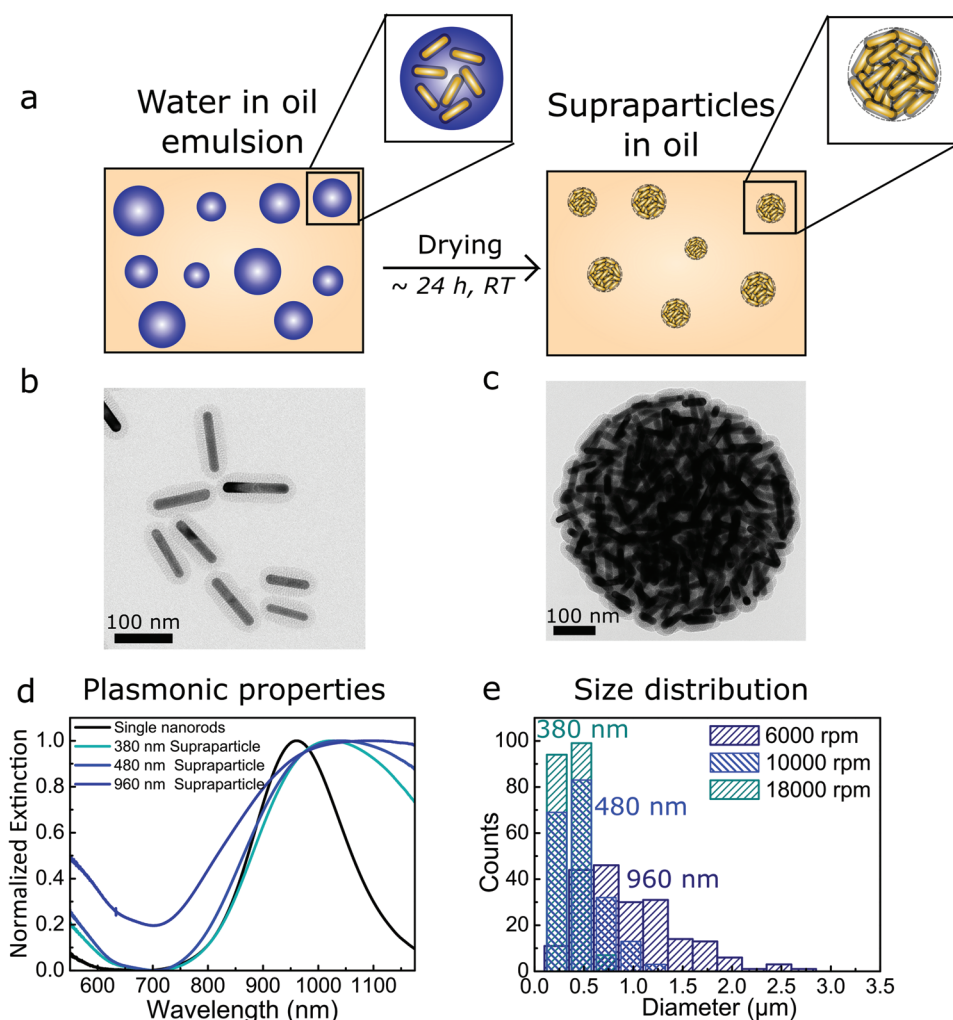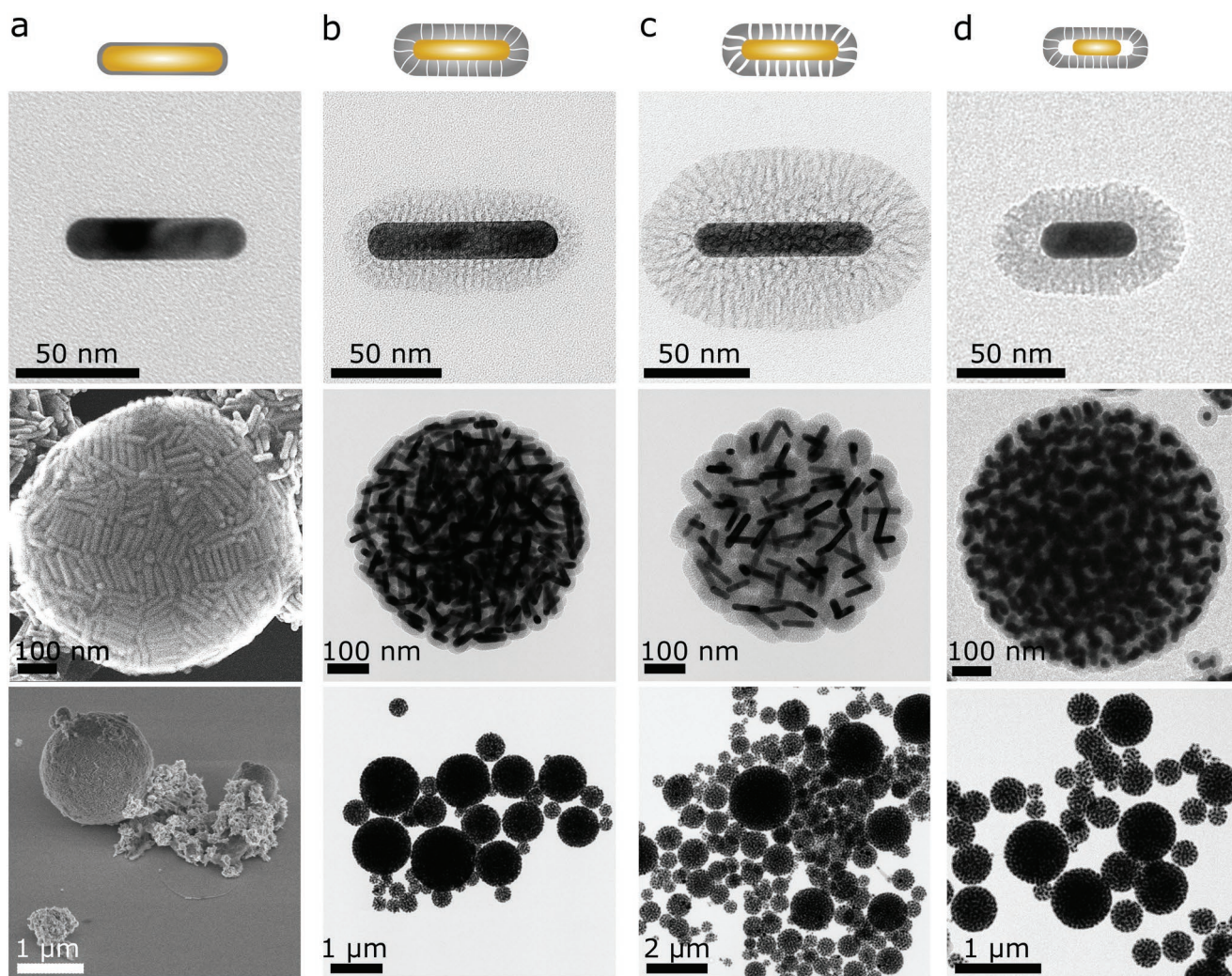
Figure 2. Self-assembly of silica-coated AuNRs into spherical supraparticles. a) Schematic representation of the assembly process: an aqueous dispersion of Au@SiO$_2$ NRs was added to a larger oil phase consisting of hexadecane with 1 wt% SPAN80. After emulsification, the water droplets were slowly dried at room temperature (RT) for ≈24 h, leading to the formation of spherical supraparticles. b) TEM image of 18 nm thick mesoporous silica-coated AuNRs before and c) after self-assembly. d) VIS-NIR spectra of the non-assembled Au@SiO$_2$ NRs (black) and self-assembled as supraparticles with an average assembly size of 380, 480, and 960 nm (blue). e) Histogram of the diameters of the supraparticles prepared by using different mixing speeds in the emulsification process (6000–18000 rpm). Extended size distributions of the supraparticles and emulsion droplets are available in Figure S5, Supporting Information.

by dividing the initial droplet volume and final supraparticle volume (Figure S5, Supporting Information) matches the expected volume fraction (≈0.2 vol%), indicating that indeed most NRs assembled into supraparticles. This is in contrast to the assembly of CTAB-stabilized rods, which yields a substantial number of non-assembled NRs (Figure S6, Supporting Information). Assembling AuNRs with reduced core size allowed further tuning of the LSPR, interparticle coupling, and porosity of the resulting Au@SiO$_2$ assemblies (Figure 3d). The etched AuNRs were obtained via oxidative etching of Au@SiO$_2$ NRs, resulting in both larger interparticle distances compared to non-etched Au@SiO$_2$ NR assemblies, and less coupling between the LSPRs of the individual rods as confirmed by the VIS-NIR spectra (Figure S7–8, Supporting Information). Hence, the interparticle distance and plasmonic coupling can be tuned via the silica shell thickness as well as by reducing the Au core size via oxidative etching.

2.3. Correlating SERS Performance and Assembly Structure

The internal interparticle distances and the porosity of the supraparticles strongly impact the performance of the Au@SiO$_2$ NR assemblies in surface-enhanced Raman spectroscopy (**Figure 4**). Figure 4a outlines our SERS-EM methodology to correlate the structural properties of the assemblies with their SERS performance, extending the 2D correlative imaging approach of Duyne et al. on single nanoparticle systems[49,50] to the (3D) characterization of larger, 3D particle ensembles. Prior to the SERS measurements, the supraparticles were washed with hexane to remove the organics used in the assembly process (SPAN80, hexadecane). The Raman spectrum in Figure S9, Supporting Information confirms that the Au surface of the Au@SiO$_2$ NRs supraparticles was accessible and that no Raman signal from organic residuals was detected. Next, the supraparticles were drop-casted on a silicon wafer, dried, and

ADVANCED
SCIENCE NEWS
www.advancedsciencenews.com

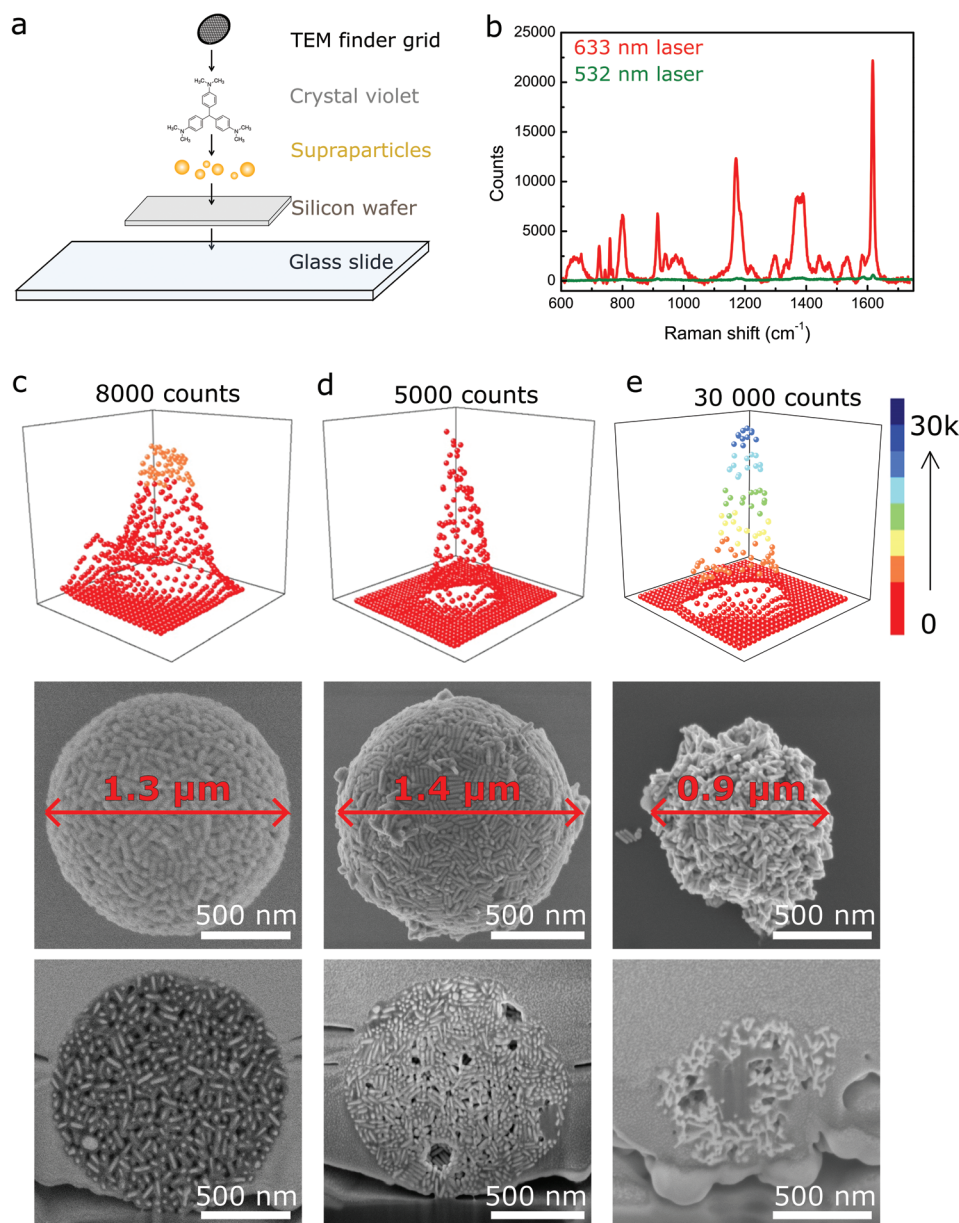ADVANCED
FUNCTIONAL
MATERIALS
www.afm-journal.de

Figure 3. Array of supraparticles obtained via self-assembly of differently silica-coated gold nanorods. Electron microscopy images of a 2 nm thin (a), 18 nm mesoporous (b) and 35 nm mesoporous (c) silica-coated AuNRs (core size = $95 \pm 8 \times 17 \pm 2$ nm), and 18 nm mesoporous (d) silica-coated etched AuNRs (core size = $43 \pm 8 \times 20 \pm 2$ nm). The top row of EM images shows the individual Au@SiO$_2$ NRs, the middle, and bottom rows show the corresponding supraparticles. All images were acquired in bright field mode in the TEM, except the middle and bottom image in (a) which were acquired with a secondary electron detector in a TEM and SEM, respectively.

exposed to a 1.0 µM crystal violet (CV) in an ethanol solution, after which the silicon wafer was placed on a glass slide and a TEM finder grid (without polymer/carbon film) was placed on top. CV was specifically chosen as a probe molecule to compare our study to earlier work on AuNR assemblies by Liz-Marzán et al.[30,32] The TEM finder grid-enabled easy relocation of the supraparticles in the electron microscope after their SERS properties had been studied. In all Raman measurements, a 633 nm laser was used, which gave a ≈50x higher Raman signal compared to a 532 nm laser (Figure 4b). This large difference is due to the fact that 633 nm laser light matches an absorption band of crystal violet and therefore leads to surface-enhanced resonant Raman scattering.[32] An overview of the vibrational modes of the crystal violet probe molecules is provided in the SI (Table S1, Supporting Information).

In Figure 4c–e the 2D Raman measurements and corresponding focused ion beam-scanning electron microscopy (FIB-SEM) images of a ≈1.4 µm large supraparticle consisting

of 18 nm mesoporous silica-coated AuNR, and a 1.3 and 0.9 µm large supraparticle consisting of 3 nm thin microporous silica-coated AuNRs are shown. The 2D Raman maps show the intensity of the Raman signal at a Raman shift of 1617 cm^{-1} as a function of the x and y sample position. The exterior and interior of the corresponding supraparticles were visualized using SEM and FIB-SEM, respectively. The results in Figure 4 confirm that all structures successfully enhanced the Raman signal of crystal violet, where the thin microporous silica-coated supraparticle with a disordered structure gave the largest enhancement and a maximum intensity of 30 000 counts at 1617 cm^{-1}. Despite the smaller assembly size, the non-spherical assembly exhibited a better Raman performance compared to the spherical, 1.3 µm supraparticle composed of the same type of Au@SiO$_2$ NRs. The FIB-SEM analysis revealed that the main difference between these supraparticles was the assembly structure, where the assembly in Figure 4e had a more open and disordered structure, whereas the Au@SiO$_2$

**ADVANCED
SCIENCE NEWS**

www.advancedsciencenews.com

**ADVANCED
FUNCTIONAL
MATERIALS**

www.afm-journal.de

Figure 4. Correlative Raman and electron microscopy measurements showing the impact of porosity and interparticle distance on the SERS performance of the Au@SiO$_2$ NR supraparticles. a) Schematic overview of the sample preparation for the Raman measurements. b) Raman signal of crystal violet on a supraparticle consisting of thin silica-coated AuNRs, recorded with a 532 nm and 633 nm laser (0.07 mW). c–e) SERS performance and corresponding (FIB)-SEM images of Au@SiO$_2$ NR supraparticles containing 18 nm thick mesoporous silica (c) and 3 nm thin microporous silica (d-e) coated AuNRs. Top: 2D Raman measurements showing the intensity of the Raman signal of crystal violet at 1617 cm^{-1}. The values 8000, 5000, and 30 000 indicate the maximum number of counts detected in c, d and e, respectively. Middle: SEM images of the corresponding supraparticles. Bottom: the same supraparticles as above sliced with FIB-SEM (after locally embedding the particles in a Pt layer) showing the interior of the supraparticles. The Raman measurements were recorded with a 633 nm laser, 0.07 mW laser power, 50× air objective (NA= 0.75, spot size ≈1 µm). The 2D maps were a collection of spectra recorded as a function of the *x* and *y* position with a step size of 0.2 µm. The FIB-SEM analysis was performed after the Raman measurements were conducted.

NRs were more closely packed in the assembly in Figure 4d. The latter structure was less porous, which likely hampered the diffusion of crystal violet into the assembly and thus yielded a relatively low Raman signal. The porosity of the supraparticle in Figure 4c consisting of mesoporous silica-coated AuNRs was high, explaining the rather high Raman signal despite the much larger interparticle spacing (≈36 nm). An additional advantage of the mesoporous silica-coated AuNR supraparticles is their reproducible SERS signal in different experiments (Figure S10, Supporting Information), whereas larger fluctuations were observed for the 3 nm microporous silica-coated AuNRs.
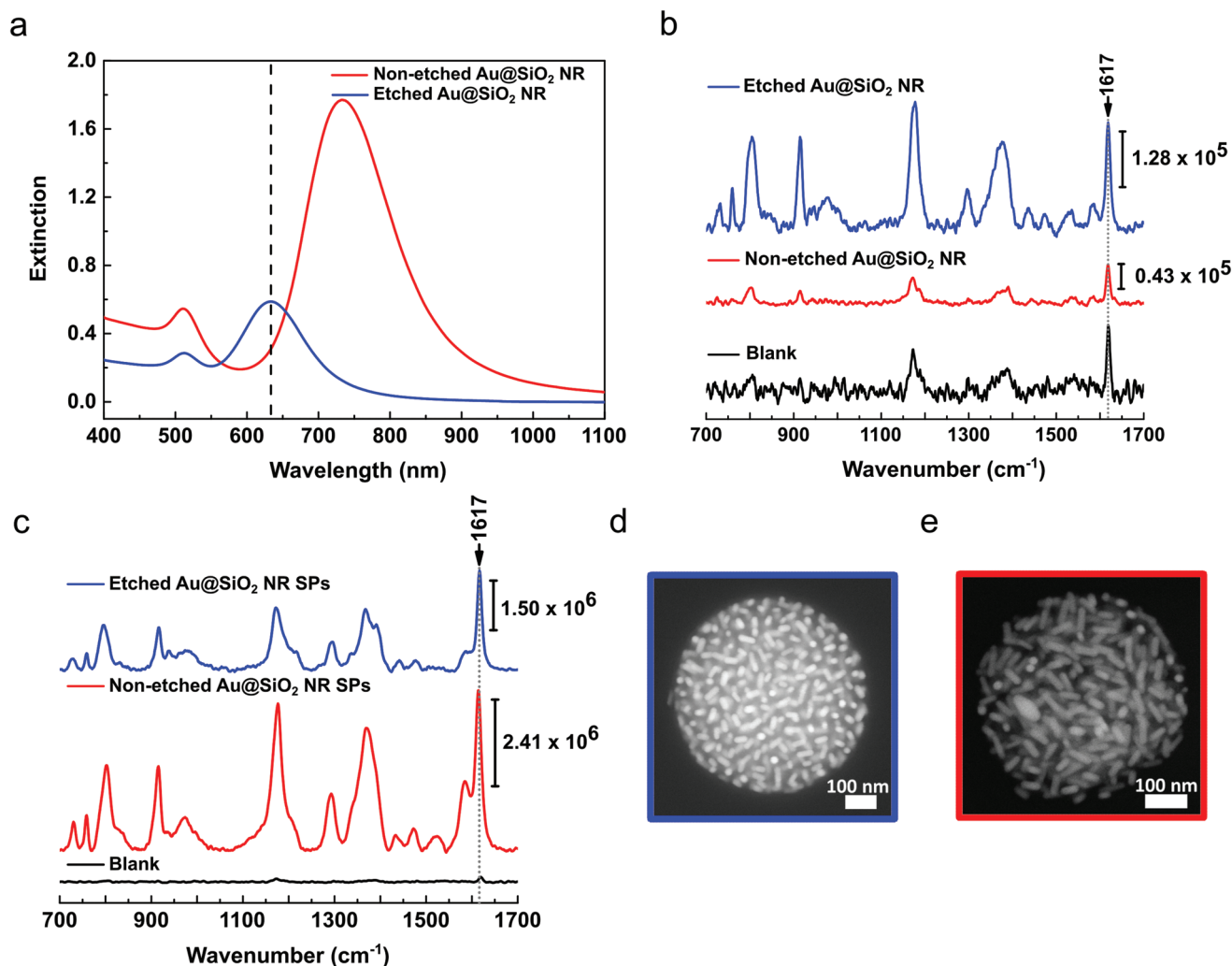
Figure 5. SERS performance of etched versus non-etched Au@SiO$_2$ NRs and their supraparticles. a) UV-VIS spectra of Au@SiO$_2$ NR before (red) and after etching (blue) in methanol. The vertical dashed line represents the excitation wavelength (633 nm) used in the SERS measurements. b) SERS spectra of 1 µM crystal violet in a 3:1 (by volume) ethanol water mixture in the presence of non-assembled Au@SiO$_2$ NR, etched (blue) and non-etched (red). The EF for the etched and non-etched Au@SiO$_2$ NRs was 1.28×10^5 and 0.43×10^5, respectively. c) SERS spectra of 1 µM crystal violet analyte in the presence of non-etched and etched Au@SiO$_2$ NR supraparticles (SPs) dried on Si-wafer. The EFs for the etched and non-etched Au@SiO$_2$ NR supraparticles were 1.50×10^6 and 2.41×10^6, respectively. d,e) SEM images of the corresponding etched (d) and non-etched Au@SiO$_2$ NR suprapar-ticle of size 611 nm and 616 nm, respectively. The Raman measurements were performed using 1% laser power (≈0.14 mW), 1 s exposure time, and 100 accumulations.

In general, the SERS signal of CV was clearly influenced by the interparticle distance of the AuNRs in the assembly. Figure S11, Supporting Information summarizes the SERS performance of supraparticles consisting of Au@SiO$_2$ NRs with a 3, 18, or 35 nm thick mesoporous silica shell. The maximum intensity between 1616 and 1618 cm^{-1} increased with decreasing silica shell thickness. Thus, smaller interparticle distances led to a steep increase in the Raman signal. Such enhancements likely arise due to the presence of interparticle hotspots in the assembly, which is in line with the VIS-NIR spectra showing clear plasmonic coupling between the Au@SiO$_2$ NRs with thin silica shells when assembled in supraparticles (Figure S8, Supporting Information).

The plasmonic overlap between the LSPR position of the AuNRs with the excitation wavelength of the laser used in the SERS measurements was further optimized via oxidative etching. **Figure 5** summarizes the plasmonic properties and SERS performance for etched and non-etched Au@SiO$_2$ NRs and their corresponding supraparticles. The non-etched Au@SiO$_2$ NR had a transverse and longitudinal LSPR at 512 nm and 733 nm, respectively (Figure 5a), whereas the longitudinal LSPR of the etched Au@SiO$_2$ NRs was set to 633 nm to maximize the overlap with the 633 nm laser light used in the SERS experiments. As expected, the SERS signal of 1 µM crystal violet adsorbed on etched Au@SiO$_2$ NRs was higher than on non-etched Au@SiO$_2$ NRs (Figure 5b). The SERS spectra were acquired in solution using our previously reported procedure,[42] where the spectrum shown is measured at a spot in the sample (Figure S12, Supporting Information), averaged over 100 accumulations. The enhancement factor (EF) for the

ADVANCED
SCIENCE NEWS
www.advancedsciencenews.com

ADVANCED
FUNCTIONAL
MATERIALS
www.afm-journal.de

etched and non-etched Au@SiO$_2$ NRs was quantified using the following relation:

$$EF = \frac{I_{SERS}}{I_{Raman}} \times \frac{N_{Raman}}{N_{SERS}} \tag{1}$$

where I_{SERS} and I_{Raman} are the intensity of a vibrational C–C stretching mode (1617–1619 cm^{-1}) in the surface-enhanced spectrum and Raman spectrum, respectively, and N_{SERS} and N_{Raman} are the concentration of analyte molecule sampled for SERS and Raman spectrum, respectively. The enhancement factor for non-etched and etched Au@SiO$_2$ NRs was in the range of 10^5 and was 3.0 times larger for etched compared to the non-etched Au@SiO$_2$ NRs.

Surprisingly, the SERS performance did not increase for the etched Au@SiO$_2$ NR supraparticles compared to their non-etched counterparts (Figure 5c). Rather, the Raman signal of CV was slightly higher in the presence of non-etched Au@SiO$_2$ NR supraparticles, despite the fact that these structures had less plasmonic overlap with the excitation wavelength of the laser. This trend was confirmed for a range of different supraparticles sizes (Figure S13–14, Supporting Information), and can likely be explained by a reduction of the plasmonic coupling between the etched Au@SiO$_2$ NRs in the supraparticles due to the relatively larger interparticle distances compared to the non-etched Au@SiO$_2$ NRs. Indeed, the ultraviolet-visible spectroscopy (UV-VIS) spectra of the non-assembled and assembled Au@SiO$_2$ NR confirm that the degree of plasmonic coupling between the AuNRs in the supraparticles is less for the etched Au@SiO$_2$ NR (Figure S7, Supporting Information). Even though this is an undesired effect, both the etched and non-etched Au@SiO$_2$ NR supraparticles exhibited a higher EF than the non-assembled Au@SiO$_2$ NRs: 10^6 versus 10^5, respectively. When normalizing the EF for the number of rods contributing to the SERS signal, the SPs outperform the non-assembled NRs by a factor of 10^3, indicating that the SERS performance of Au@SiO$_2$ NRs is strongly enhanced when assembling them in supraparticles.

3. Discussion

The Au@SiO$_2$ NR supraparticles presented in this study have several advantages over template-directed methods. Our emulsion evaporation method allows facile control over the assembly size via water droplet size and the concentration of the Au@SiO$_2$ NRs dispersed in the droplets (Figure 2e). In this work, the mixing speed was varied to obtain assemblies with different average sizes. The control over the size and monodispersity of the supraparticles can further be improved through precise tuning of the droplet size in a microfluidic setup.[51,52] Importantly, mass- and heat transport limitations of the analytes in the Au@SiO$_2$ NR assemblies can be mitigated as the assembly size can easily be optimized. The tunable porosity of the silica shells also enables facile uptake of the analytes ensuring that not only the AuNRs at the assembly surface but all AuNRs in the assembly contribute to the SERS performance, which is a known problem in template-directed assemblies of uncoated AuNRs.[32] Furthermore, tuning the pore size as shown in Figure 3 allows for selective SERS of molecules of a certain size.[53] Our emulsion-based assembly method yielding supraparticles well-dispersed in solution is advantageous for local sensing applications: the supraparticles can easily be drop-casted from solution on a wide variety of surfaces which is not straightforward with assemblies grown in templates. Further modification of the supraparticles via wet chemical methods would make them suitable for biomedical applications, e.g. by coating them with a protective layer or specific functionality.[54] Finally, it is worthwhile to note that the experimental approach described in this work allows for a direct comparison between experimental measurements and theoretical predictions of the SERS performance of plasmonic particle assemblies. Using our correlative SERS-EM approach (Figure 4a), detailed structural analysis with FIB-SEM tomography or TEM tomography (Movie S1, Supporting Information) renders all particle coordinates and interparticle distances of individual supraparticles used in SERS experiments.[48,55] The experimental particle coordinates can then be used as input for calculations to compute the strength of the interparticle hotspots and the theoretical SERS performance.[32]

Compared to previous work on template-directed AuNR assemblies our supraparticles show similar SERS performance for much smaller ensembles, and hence for a considerably lower number of Au@SiO$_2$ NRs. The more disordered, 0.94 μm supraparticle, which also had more surface roughness, consisting of the 3 nm thin silica-coated AuNRs amplified the Raman signal of crystal violet to a maximum of 30 000 counts at 1617 cm^{-1} (Figure 4e). This is significantly higher compared to assemblies of uncoated AuNRs[30,32] and comparable AuNRs crystals infiltrated with mesoporous silica,[30] which had a signal of 700–1300 and 25 000 counts at 1618–1632 cm^{-1}, respectively. However, the colloidal crystals in ref[30] contained considerably more AuNRs and the assembly had a height of about 1.4-2.0 μm, and thus had more particles in the laser spot when performing the Raman measurements compared to the supraparticles depicted in Figure 4. The measurement conditions were slightly different: in refs[30,32] a 100x objective with numerical aperture (NA) = 0.85, 633 nm laser, 0.15 mW and 0.1–0.5 s integration time were used, and in our measurements a 50x objective with NA = 0.75, 633 nm laser, 0.07 mW and 1.0 s integration time. Although this complicates quantitative comparisons, it suggests that the supraparticles in this work are able to give similar SERS performances even though they consist of considerably less particles. The supraparticles are therefore likely to be suitable for sensing biological analytes and sensing extremely low analyte concentrations (≤10^{-15}) as demonstrated for the template-grown assemblies.[56]

As expected, the interparticle distance of the AuNRs in the supraparticles significantly impacts the SERS performance of the assemblies. Our results show that the Raman signal of crystal violet decreased with increasing silica shell thickness, and thus with increasing interparticle distance (Figure S3, Supporting Information). Yet, decreasing the interparticle distance too far will lead to diffusion limitations, as demonstrated for uncoated AuNR assemblies where only the outer layer of rods contributes to the SERS performance.[32] Surprisingly, the supraparticles with Au@SiO$_2$ NRs with d_{shell} = 18 nm still enhanced the Raman signal more strongly compared to the rods with d_{shell} = 35 nm which indicates that the Au@SiO$_2$ NRs

with d_{shell} = 18 nm are weakly optically coupled and that there is still some overlap of the surface plasmons of the individual AuNRs. This is supported by the broadening and redshift of the LSPR peak in the VIS-NIR spectra (Figure 2d). For dimers of AuNRs, the plasmonic coupling was reported to exponentially decay for interparticle separations (d_{gap}) of 0.1–1 times the rod length (L) and complete decoupling of the rods when d_{gap} = $3L$.[23] This means that even for the 18 nm thick silica-coated AuNRs with a $d_{gap} \approx 36$ nm (0.4L), plasmonic coupling can still occur, which explains why the Raman signal is higher for the supraparticles consisting of Au@SiO$_2$ NRs with d_{shell} = 18 nm compared to d_{shell} = 35 nm. Previously, the dependence of the SERS performance on the interparticle distance has been observed for dimers of Ag spheres coated with silica shells of a different thickness. However, in that case, the enhancement factor already dropped drastically at $d_{gap} \approx 10$–15 nm.[38]

The thin silica-coated plasmonic NPs have the potential for Shell-Isolated Nanoparticle-Enhanced Raman Spectroscopy (SHINERS) applications, for instance in monitoring catalytic reactions in situ.[2–4,45] The current thin silica-coated Au@SiO$_2$ NRs were not completely closed and part of the gold surface was still accessible. For SHINERS applications the silica shell should be made pinhole-free to prevent the gold surface from participating in the catalytic process. This can be done by growing a thin additional Stöber layer on top of the 3 nm silica coating as demonstrated in Figure 1b, or by giving the silica shell a thermal treatment to condensate the silica[22] and decrease the porosity of the shell. Such a thermal treatment would also increase the stability of the thin shell in water and improve the assembly of these rods, preventing the formation of aggregates. These aggregates could also be caused by Van der Waals attractions between the AuNRs.[58] We estimated the Van der Waals attraction between the 3 nm thin silica-coated AuNRs to be on the order of –7 k_BT (see SI for details) which is substantial. Still, it is possible that in our experiments the Van der Waals attractions between the gold cores were completely screened by electrostatic repulsion between the silica shells. The lack of clear evidence for a strong preference for side-to-side arrangement (that is extremely favorable for attractive rods) in the electron microscopy images, indeed indicates that attractions did not play a crucial role in the self-assembly.

Comparing the SERS performance of the non-assembled etched and non-etched Au@SiO$_2$ NRs, and corresponding supraparticles revealed that the spectral overlap between the LSPR of the AuNRs and the excitation laser light had a lower impact than expected (Figure 5). The on-resonance excitation of plasmonic AuNRs is known to be an important parameter in maximizing the enhancement of the Raman signal from nearby molecules. Yet, Khlebstov et al.[59] recently reported that the dependence of SERS enhancement on the plasmonic resonance wavelength of AuNRs is lower than expected from theory, which is in line with our non-assembled Au@SiO$_2$ NR results. The absence of strong differences in enhancement factor between etched and non-etched Au@SiO$_2$ NR supraparticles was likely due to a reduction of the plasmonic coupling-, and hence reduction of overlapping of plasmonic hotspots between the etched Au@SiO$_2$ NR due to the relatively larges interparticle distances. The enhancement factor of $\approx 10^5$ measured for the non-assembled nanorods in this study is comparable with other studies using Au@SiO$_2$ NRs.[60,61] Additionally, it should be noted that the mesoporous silica coating around the AuNRs increases the uptake and residence time of analyte molecules near the gold surface resulting in improved SERS signal magnitudes.[61]

The parameters critical to further optimize the supraparticles for SERS applications are related to the assemblies porosity, the wetting of the probe molecule solution on and into the supraparticle, and the individual- and collective plasmonic properties of the nanoparticles. Control over these parameters can be achieved via the porosity and chemical functionalization of the silica shell, the size and shape of the individual gold nanoparticles, and the interparticle distance and orientation. Introducing mesopores in the silica shell enables better mass transport compared to microporous silica shells. However, this typically comes at the cost of an increased silica shell thickness (often above 10 nm), and hence less plasmonic coupling between the NRs. It will therefore be worthwhile to explore synthesis protocols for growing mesoporous silica shells of only a few nm thick to ensure better plasmonic coupling between the NRs while retaining the mesoporosity.[62] The surface functionalization of the silica shell determines the wetting of the solution containing the probe molecules. In this work, we demonstrated the use of hydrophilic supraparticles for polar probe molecule solutions. However, it is also possible to prepare hydrophobic supraparticles for apolar solutions through functionalization of the silica shells with octadecyl trimethoxysilane and self-assembly in an oil-in-water instead of a water-in-oil emulsion.[48,55] The plasmonic properties of the individual nanoparticles can be tuned via their size and shape. We showed how to modify the AR of the NRs via oxidative etching to match the excitation wavelength of the laser (Figure 5). Finally, the interparticle distance and interparticle orientation are important in tuning the collective plasmonic properties. Stronger plasmonic hotspots between the NRs can be created by decreasing interparticle distance, but this reduces the porosity of the assembly and can cause mass transport limitations. Hence, shorter interparticle distances do not always lead to improved performances. Inducing orientational order in a tip-to-tip alignment through the formation of smectic order inside the supraparticles, could further enhance the SERS performance provided that a suitable (near) infrared laser matching the red-shifted LSPR of the oriented assemblies is used.[57]

4. Conclusions

This work presents a novel design of gold nanorod supraparticle assemblies for sensing applications. The porosity, interparticle distance, and optical properties of these assemblies can be tuned via the properties of the silica shell and core size of the individual Au@SiO$_2$ NRs, whereas the size of the assemblies can easily be varied via the size of water droplets in the emulsion. Our correlative SERS-EM methodology revealed that the interparticle distance as well as the ensemble porosity drastically affect the SERS performance, where a more open, porous assembly consisting of 3 nm thin silica-coated AuNRs showed the best Raman performance. The decreased interparticle distance in these assemblies gave rise to plasmonic hotspots

**ADVANCED
SCIENCE NEWS**

www.advancedsciencenews.com

**ADVANCED
FUNCTIONAL
MATERIALS**

www.afm-journal.de

between the AuNRs, which more strongly amplified the Raman scattering of the analyte molecules. Additionally, our results show that the impact of the overlap of the LSPR of the Au@SiO$_2$ NRs and the laser light used in the SERS measurements was less prominent than expected in the case of non-assembled particles and negligible for the supraparticles. Altogether, our work demonstrates that silica-coated gold nanorod supraparticles are promising materials for sensing and that there is still a wide parameter space to explore in further optimizing these assemblies for SERS applications.

5. Experimental Section

Chemicals: All chemicals were used as received without further purification. Hexadecyltrimethylammonium bromide (CTAB, >98.0%) and sodium oleate (NaOL, >97.0%) were purchased from TCI America. Hydrogen tetrachloroaurate trihydrate (HAuCl$_4$·3H$_2$O) and sodium hydroxide (98%) were purchased from Acros Organics. L-Ascorbic Acid (BioXtra, ≥99%), hydrogen peroxide (H$_2$O$_2$, 30 wt% in H$_2$O), hydrochloric acid (HCl, 37 wt% in water), silver nitrate (AgNO$_3$, ≥99%), sodium silicate solution (≥27% SiO$_2$ basis, Purum ≥10% NaOH), tetraethyl orthosilicate (TEOS, 98%), decane (≥99.5%), pyridine (≥99%) and crystal violet (CV, ≥90%) were purchased from Sigma-Aldrich. Absolute ethanol and hexadecane (≥99.0%) were purchased from Merck. SPAN80 and sodium borohydride (NaBH$_4$, 99%) were purchased from Fluka. Methanol was purchased from Interchem (≥99.85%). Ultrapure water (Millipore Milli-Q (MQ) grade) with a resistivity of 18.2 MΩ was used in all of the experiments. All glassware for the AuNR synthesis was cleaned with fresh aqua regia (HCl/HNO$_3$ in a 3:1 volume ratio), rinsed with large amounts of water, and dried at 100 °C before use.

Gold nanorod synthesis: The gold nanorod synthesis was performed according to the procedure of Ye et al.[50] The seed solution consisted of 10 mL 0.10 M CTAB and 51 μL 50 mM HAuCl$_4$ to which 1.0 mL 0.0060 M NaBH$_4$ was added while stirring vigorously for 2 min (≈1200 rpm). For the aqueous growth solution, 7.0 g CTAB and 1.24 g NaOL were dissolved in 250 mL MQ H$_2$O. For AR = 5.5, 250 mL 1.0 mM HAuCl$_4$, 7.2 mL 10 mM AgNO$_3$, 3.0 mL HCl (37 wt%, 12.1 M), 1.25 mL 0.064 M ascorbic acid in water and 0.80 mL aqueous seed solution were added, while stirring at 350 rpm (revolutions per minute) in a 30 °C water bath. For AR = 3.4, 250 mL 1.0 mM HAuCl$_4$, 4.8 mL 10 mM AgNO$_3$, 2.10 mL concentrated HCl (37 wt%, 12.1 M), 1.25 mL 0.064 M ascorbic acid in water and 0.8 mL aqueous seed solution were added. Then reaction mixtures were left under static conditions overnight in a 30 °C water bath. Thereafter, the rods were washed with 120 mL H$_2$O via centrifugation at 8000 rcf (relative centrifugal force) for 30 min and stored in 36 mL 5.0 mM CTAB in water. The resulting high aspect ratio rods had an average length (L_{Au}) and standard deviation of 95 ± 8 nm, diameter (D_{Au}) of 17 ± 2 nm, and aspect ratio (AR_{Au}) of 5.5 ± 0.76. The low aspect ratio rods had an average length (L_{Au}) and standard deviation of 64 ± 8 nm, diameter (D_{Au}) of 19 ± 1 nm, and aspect ratio (AR_{Au}) of 3.4 ± 0.56.

Silica Coating: Thin silica shells: For the synthesis of thin, homogeneous silica shells around AuNRs the synthesis protocol of Li et al. was modified.[45] No coupling agent was used as it is not necessary for the silica shell growth on CTAB stabilized AuNRs and high temperatures (90 °C) were avoided as this leads to aggregation of the AuNRs. The shell thickness of the thin shells was tuned via the reaction time or via the reaction temperature. First, 2.0 mL AuNRs in 5.0 mM CTAB H$_2$O dispersion (λ_{LSPR} = 964 nm, Ext = 1.42 when diluted 40x in H$_2$O) were centrifuged at 9000 rcf for 10 min, redispersed in 22 mL MQ H$_2$O and transferred to a 40 mL glass vial. While vigorously stirring at room temperature (RT), 3.5 mL sodium silicate (0.54 wt% SiO$_2$, ≈0.12 M sodium silicate) was added. After 5 min of stirring, the reaction vial was placed in a 60 °C water bath. After 15 min, 30 min, 1 h, 2 h, and 4 h part of the reaction mixture was removed from the reaction

vial, washed two times with 6 mL H$_2$O, 2 times with 6 mL EtOH and redispersed in 2.0 mL EtOH for storage. Alternatively, the shell thickness was altered via the reaction temperature. In that case, the reaction mixture was divided into three batches, which were placed in a 20, 40, or 60 °C water bath. After 2 h, the reaction mixtures were removed from the reaction vial, washed 2 times with 6 mL H$_2$O, 2 times with 6 mL EtOH and redispersed in 2.0 mL EtOH for storage. It should be noted that these thin silica coatings, especially when grown at low temperatures (20—40 °C), were unstable in water and had the tendency to dissolve, leading to aggregation of the gold nanorods. The silica-coated rods should therefore always be stored in ethanol.

Mesoporous silica coating with 2.5 nm pores: For the mesoporous silica coating the procedure of Gorelikov et al. was used,[43] which typically yields AuNRs with a 15–20 nm coating containing 2.5 nm wide mesopores. The silica coating was performed on a 10 mL scale. 2.0 mL of the stored AuNRs in 5.0 mM CTAB water were used, to which 1.0 mL 5.0 mM aqueous CTAB solution, 7.0 mL MQ H$_2$O and 100 μL 0.10 M NaOH were added. While magnetically stirring at 300 rpm in a 30 °C water bath, three times 30 μL 0.90 M TEOS in EtOH were added with a 45 min time interval. After 48 h, the Au@SiO$_2$ NRs were centrifuged at 8000 rcf for 30 min, washed with water and ethanol, and redispersed in 2.0 mL EtOH for storage.

Mesoporous silica coating with increased porosity: The pore size of the mesopores in the silica shells was increased by adding a mixture of decane and toluene, which swells the CTAB micelles. We modified the protocol of Gorelikov et al.[31] in the following way. To 2.0 mL of the stored AuNRs in 5.0 mM CTAB water, 2.0 mL ethylene glycol and 6.0 mL 5.0 mM CTAB water were added. Next, 100 μL 0.10 M NaOH and 101 μL decane were added. The mixture was stirred at ≈300 rpm for 2 h in a 70 °C water bath. Thereafter, 12.8 μL toluene was added. After 2 h of stirring, three times 30 μL 0.90 M TEOS in EtOH were added with a 45 min time interval between the additions. The reaction mixture was left overnight at 50 °C. The rods were washed with 8 mL H$_2$O, 8 mL EtOH and redispersed in 2.0 mL EtOH for storage. Note that the addition of ethylene glycol is crucial to obtain a homogeneous shell growth.

Removal of the CTAB from the mesopores: To remove the CTAB and open the mesopores of the silica-coated AuNRs, the Au@SiO$_2$ NRs were washed with 0.10 M HCl in EtOH. To 2.0 mL dispersion of Au@SiO$_2$ NRs in EtOH, 17 μL of concentrated HCl (12.1 M in water) was added such that the HCl concentration in EtOH was 0.10 M. The acidified dispersion was sonicated for 30 min at RT. Next, the Au@SiO$_2$ NRs were centrifuged at 8000 rcf for 15 min, washed three times with 2 mL EtOH to remove the HCl. Thereafter, the rods were redispersed in 1.0 mL EtOH.

Non-porous Stöber silica coating: To increase the shell thickness of the thin silica-coated AuNRs a subsequent growth step was carried out. To 10 mL dispersion (8 mL EtOH, 2 mL H$_2$O) of 3 nm silica-coated AuNRs (Ext = 4.0 when 4x diluted in EtOH), 40 μL of a 0.10 M NaOH solution was added, immediately followed by the addition of 100 μL 0.045 M TEOS in EtOH. The reaction was left overnight and washed twice with 10 mL H$_2$O (7000 rcf × 15 min) and redispersed in 10 mL EtOH for storage.

Oxidative Etching: The oxidative etching was carried out following our previously published procedure.[42] To 15 mL silica-coated AuNRs (λ_{LSPR} = 733 nm, Ext = 1.7 when 20× diluted in MeOH) in MeOH, 300 μL HCl (37 wt%, 12.1 M in water) and 300 μL 50 mM H$_2$O$_2$ in MeOH (containing 0.19 M H$_2$O) were added, resulting in a final HCl and H$_2$O$_2$ concentration of 0.24 M and 1.0 mM, respectively. Thereafter, the reaction was immediately heated in a 60 °C oil bath while magnetically stirring at 400 rpm. After 97 min the reaction was quenched with 25 mL of fresh MeOH. The longitudinal LSPR peak position of the etched AuNRs in MeOH had shifted from 733 to 633 nm. The particles were centrifuged at 8000 rcf for 30 min. Next, the particles were washed with 20 mL MeOH, 20 mL H$_2$O and redispersed in 15 mL EtOH.

Self-Assembly: The self-assembly of the silica-coated AuNRs into spherical clusters was done via a water-in-oil emulsion method, which is different from the previously reported oil-in-water method described

**ADVANCED
SCIENCE NEWS**

www.advancedsciencenews.com

**ADVANCED
FUNCTIONAL
MATERIALS**

www.afm-journal.de

by Nijs et al.[47,48] Typically, 300 µL of the silica-coated gold nanorods as stored in ethanol were centrifuged at 8000 rcf for 5 min and redispersed in 100 µL MQ H_2O (≈0.2 vol% particles in water). This aqueous rod suspension was then added to a 40 mL glass vial containing 5.0 mL hexadecane with 1 wt% SPAN80. The mixture was emulsified by mixing for 2 min with a Turrax mixer (IKA T25 digital, Ultra Turrax) of which the speed was set to 6000, 10 000, or 180 000 rpm depending on the desired droplet size. Afterwards, the vial was covered with teflon tape. With a needle, a hole was made in the teflon tape after which the vial was placed in a vortex shaker (IKA KS 260 basic). The emulsion was left to dry for 1–1.5 day while shaking at 300 rpm. The resulting supraparticles were centrifuged at 150–300 rcf for 5 min and redispersed in 1.0 mL toluene or hexane.

Raman Measurements: The Raman measurements were performed using a Renishaw Raman microscope equipped with a RL532C50 and RL633 nm HeNe laser giving 532 and 633 nm light, respectively, with a maximum power of ≈12.5 mW. For the non-assembled particle SERS measurement, a 3:1 (by volume) ethanol/water dispersion containing the Au@SiO$_2$ NRs with a fixed Au atom concentration and crystal violet concentration of 1.0 µM was loaded to a glass capillary, sealed, and mounted on a glass slide with UV-glue. The Au concentration was 0.30 mM and 0.26 mM for non-etched and etched Au@SiO$_2$, respectively, as determined with inductively coupled plasma mass spectrometry. Then the glass slide was mounted on the Renishaw Raman microscope. For Raman measurements, a 50x air objective with NA = 0.75 and a laser spot size of about 1 µm was used. During the SERS measurements 10 different spots in each sample were probed, where 100 accumulations with a laser power of 1% (≈0.14 mW), exposure time of 1 s was taken at each spot. The sample preparation for the Raman measurements with the supraparticles was done as schematically shown in Figure 2. First, the supraparticles were drop-casted on a piece of silicon wafer. Next, the silicon wafer was placed in an ethanol solution containing 1.0 µM crystal violet (CV) for 1 h. Thereafter, the wafer was dried and placed on a glass microscope slide. With scotch tape, a copper 200 mesh TEM finder grid was placed on top of the silicon wafer (the copper grid did not contain a polymer film). The glass slide was mounted on a Renishaw Raman microscope. For the Raman measurements, a 50x air objective with NA = 0.75 and a laser spot size of about 1 µm was used. Typically, a laser power of 0.5% (≈0.07 mW), exposure time of 1 s, and 1 accumulation were used. The step size in the 2D Raman mapping experiments was 0.2 µm. For the etched and non-etched Au@SiO$_2$ NRs (with an aspect ratio of 3.4), a laser power of 1% (≈0.14 mW), exposure time of 1 s, and 100 accumulations were used at different spots. The pyridine Raman measurements were carried out as follows: 10 µL of the Au@SiO$_2$ NRs were dried on a silicon wafer, which was placed on a glass microscope slide. Next, 20 µL of 10 mM pyridine in H_2O solution and a glass slide were put on top. For the measurements, a laser power of 10% (≈0.13 mW), exposure time of 10 s, and 1 accumulation were used. For blank measurement, 0.1 M crystal violet in ethanol was used and Raman spectra were obtained using a 50x air objective with NA = 0.75, a laser spot size of about 1 µm, a laser power of 1% (≈0.14 mW), exposure time of 1 s and 100 accumulations were used.

Number of rods contributing to the SERS signal: For the non-assembled NRs ≈3 × 10^8 NRs are contributing to the measured SERS signal (Au concentration = 0.3 mM, capillary thickness = 0.4 mm, laser spot size ≈1 µm). For a supraparticle with a diameter of 1 µm and a rod density of 2.7 × 10^{15} rods per cm^3 (as estimated from the tomography data set, 241 rods in a supraparticle with a diameter of 555 nm) ≈1.4 × 10^3 NRs contribute to the SERS signal.

Characterization: The individual silica-coated AuNRs and their assemblies were analyzed with TEM (transmission electron microscope) on a FEI Talos F200X or FEI Tecnai 20FEG operated at 200 kV. The Tecnai20FEG microscope was equipped with a secondary electron detector enabling the analysis of the surface structure of the supraparticles. The supraparticles used for Raman spectroscopy were characterized using a Helios Nanolab G3 UC focused ion beam-scanning electron microscope (Thermo Fisher Scientific) microscope.

The optical properties of the silica-coated AuNRs in ethanol and AuNR supraparticles in toluene were measured using a Bruker Vertex 70 FTIR/VIS spectrophotometer and a PerkinElmer UV/VIS Lambda 365 spectrophotometer.

Statistical Analysis: Extinction spectra (Figures 2d, S7 & S8, Supporting Information) were normalized to 1. ImageJ software was used to measure the (supra)particle size, which is reported as an average of 100–200 (supra)particles. All the particle sizes were expressed as mean ± standard deviation. Statistical analysis was performed using Origin software (9.1) version.

Supporting Information

Supporting Information is available from the Wiley Online Library or from the author.

Conflict of Interest

The authors declare no conflict of interest.

Author Contributions

J.E.S.v.d.H., H.G. contributed equally to this work. A.v.B. supervised the project. J.v.d.H. and H.G. synthesized the samples, acquired the SERS data and conducted the TEM imaging. J.v.d.H. acquired the TEM tomography data. M.B. and D.W. contributed the (FIB)SEM imaging. J.v.d.H. and H.G. wrote the manuscript with contributions of M.B., D.W., P.d.J. and A.v.B.

Data Availability Statement

The data that support the findings of this study are available from the corresponding author upon reasonable request.

[1] X. M. Qian, S. M. Nie, *Chem. Soc. Rev.* **2008**, *37*, 912.

[2] H. Zhang, C. Wang, H. L. Sun, G. Fu, S. Chen, Y. J. Zhang, B. H. Chen, J. R. Anema, Z. L. Yang, J. F. Li, Z. Q. Tian, *Nat. Commun.* **2017**, *8*, 15447.

[3] T. Hartman, B. M. Weckhuysen, *Chem. – Eur. J.* **2018**, *24*, 3733.

[4] T. Hartman, C. S. Wondergem, N. Kumar, A. Van Den Berg, B. M. Weckhuysen, *J. Phys. Chem. Lett.* **2016**, *7*, 1570.

[5] R. E. Armstrong, M. Horáček, P. Zijlstra, *Small* **2020**, *16*, 2003934.

[6] C. Muehlethaler, M. Leona, J. R. Lombardi, *Anal. Chem.* **2016**, *88*, 152.

[7] F. Casadio, M. Leona, J. R. Lombardi, R. Van Duyne, *Acc. Chem. Res.* **2011**, *44*, 238.

[8] A. Lee, G. F. S. Andrade, A. Ahmed, M. L. Souza, N. Coombs, E. Tumarkin, K. Liu, R. Gordon, A. G. Brolo, E. Kumacheva, *J. Am. Chem. Soc.* **2011**, *133*, 7563.

[9] N. Félidj, J. Aubard, G. Lévi, J. R. Krenn, M. Salerno, G. Schider, B. Lamprecht, A. Leitner, F. R. Aussenegg, *Phys. Rev. B: Condens. Matter. Mater. Phys.* **2002**, *65*, 0754191.

[10] H. K. K. Kneipp, M. Moskovits, *Surface-Enhanced Raman Scattering* (Ed.: Claus E. Ascheron, Hans J. Koelsch), 6th ed., Springer-Verslag, Berlin Heidelberg **2006**, pp. 0303–4216.

[11] R. Contreras-Caceres, P. Dawson, P. Formanek, D. Fischer, F. Simon, A. Janke, P. Uhlmann, M. Stamm, *Chem. Mater.* **2013**, *25*, 158.

[12] M. N. Sanz-Ortiz, K. Sentosun, S. Bals, L. M. Liz-Marzán, *ACS Nano* **2015**, *9*, 10489.

[13] Y. Yang, J. Liu, Z. W. Fu, D. Qin, *J. Am. Chem. Soc.* **2014**, *136*, 8153.

[14] C. F.-L. S. Gómez-Graña, B. Goris, T. Altantzis, L. M. L.-M. E. Carbo-Argibay, A. Guerrero-Martinez, N. Almora-Barrios, N. Lopez, I. Pastoriza-Santos, J. Perez-Juste, S. Bals, G. Van Tendeloo, *J. Phys. Chem. Lett.* **2013**, *4*, 2209.

[15] J. Zheng, X. Cheng, H. Zhang, X. Bai, R. Ai, L. Shao, J. Wang, *Chem. Rev.* **2021**, *121*, 13342.

[16] C. J. Orendorff, L. Gearheart, N. R. Janaz, C. J. Murphy, *Phys. Chem. Chem. Phys.* **2006**, *8*, 165.

[17] K.-Q. Lin, J. Yi, S. Hu, B.-J. Liu, J.-Y. Liu, X. Wang, B. Ren, *J. Phys. Chem. C* **2016**, *120*, 20806.

[18] S. T. Sivapalan, B. M. Devetter, T. K. Yang, T. Van Dijk, M. V. Schulmerich, P. S. Carney, R. Bhargava, C. J. Murphy, *ACS Nano* **2013**, *7*, 2099.

[19] J. Kumar, R. Thomas, R. S. Swathi, K. G. Thomas, *Nanoscale* **2014**, *6*, 10454.

[20] M. Moskovits, *J. Raman Spectrosc.* **2005**, *36*, 485.

[21] C. Sönnichsen, B. M. Reinhard, J. Liphardt, A. P. Alivisatos, *Nat. Biotechnol.* **2005**, *23*, 741.

[22] K. D. Alexander, K. Skinner, S. Zhang, H. Wei, R. Lopez, *Nano Lett.* **2010**, *10*, 4488.

[23] A. M. Funston, C. Novo, T. J. Davis, P. Mulvaney, *Nano Lett.* **2009**, *9*, 1651.

[24] L. Scarabelli, D. Vila-Liarte, A. Mihi, L. M. Liz-Marzán, *Acc. Mater. Res.* **2021**, *2*, 816.

[25] C. Hanske, E. H. Hill, D. Vila-Liarte, G. Gonzaíez-Rubio, C. Matricardi, A. Mihi, L. M. Liz-Marzan, *ACS Appl. Mater. Interfaces* **2019**, *11*, 11763.

[26] T. Chen, M. Pourmand, A. Feizpour, B. Cushman, B. M. Reinhard, *J. Phys. Chem. Lett.* **2013**, *4*, 2147.

[27] N. Gandra, A. Abbas, L. Tian, S. Singamaneni, *Nano Lett.* **2012**, *12*, 2645.

[28] J. Langer, D. Jimenez de Aberasturi, J. Aizpurua, R. A. Alvarez-Puebla, B. Auguie, J. J. Baumberg, G. C. Bazan, S. E. J. Bell, A. Boisen, A. G. Brolo, J. Kneipp, N. A. Kotov, H. Kuang, E. C. Le Ru, H. Kwee Lee, J.-F. Li, X. Yi Ling, S. A. Maier, T. Mayerho, M. Moskovits, K. Murakoshi, J.-M. Nam, S. Nie, Y. Ozaki, I. Pastoriza-Santos, J. Perez-Juste, J. Popp, A. Pucci, S. Reich, B. Ren, et al., *ACS Nano* **2020**, *14*, 28.

[29] N. Pazos-Perez, C. S. Wagner, J. M. Romo-Herrera, L. M. Liz-Marzán, F. J. García De Abajo, A. Wittemann, A. Fery, R. A. Alvarez-Puebla, *Angew. Chemie – Int. Ed.* **2012**, *51*, 12688.

[30] C. Hamon, M. N. Sanz-Ortiz, E. Modin, E. H. Hill, L. Scarabelli, A. Chuvilin, L. M. Liz-Marzán, *Nanoscale* **2016**, *8*, 7914.

[31] R. A. Alvarez-Puebla, A. Agarwal, P. Manna, B. P. Khanal, P. Aldeanueva-Potel, E. Carbó-Argibay, N. Pazos-Pérez, L. Vigderman, E. R. Zubarev, N. A. Kotov, L. M. Liz-Marzán, *Proc. Natl. Acad. Sci. USA* **2011**, *108*, 8157.

[32] C. Hamon, S. M. Novikov, L. Scarabelli, D. M. Solís, T. Altantzis, S. Bals, J. M. Taboada, F. Obelleiro, L. M. Liz-Marzán, *ACS Photonics* **2015**, *2*, 1482.

[33] C. Hanske, G. González-Rubio, C. Hamon, P. Formentín, E. Modin, A. Chuvilin, A. Guerrero-Martínez, L. F. Marsal, L. M. Liz-Marzán, *J. Phys. Chem. C* **2017**, *121*, 10899.

[34] T. Thai, Y. Zheng, S. H. Ng, S. Mudie, M. Altissimo, U. Bach, *Angew. Chemie., Int. Ed.* **2012**, *51*, 8732.

[35] C. Matricardi, C. Hanske, J. L. Garcia-Pomar, J. Langer, A. Mihi, L. M. Liz-Marzán, *ACS Nano* **2018**, *12*, 8531.

[36] B. Chen, G. Meng, Q. Huang, Z. Huang, Q. Xu, C. Zhu, Y. Qian, Y. Ding, *ACS Appl. Mater. Interfaces* **2014**, *6*, 15667.

[37] K. Sivashanmugan, J. Der Liao, J. W. You, C. L. Wu, *Sens. Actuators, B* **2013**, *181*, 361.

[38] M. Shanthil, R. Thomas, R. S. Swathi, T. K. George, *J. Phys. Chem. Lett.* **2012**, *3*, 1459.

[39] S. Li, Q. Wan, Z. Qin, Y. Fu, Y. Gu, *J. Therm. Anal. Calorim.* **2019**, *136*, 1895.

[40] S. Li, Q. Wan, Z. Qin, Y. Fu, Y. Gu, *Langmuir* **2016**, *32*, 9180.

[41] S. Li, Q. Wan, Z. Qin, Y. Fu, Y. Gu, *Langmuir* **2015**, *31*, 824.

[42] J. E. S. Van Der Hoeven, T. S. Deng, W. Albrecht, L. A. Olthof, M. A. Van Huis, P. E. De Jongh, A. Van Blaaderen, *ACS Omega* **2021**, *6*, 7034.

[43] I. Gorelikov, N. Matsuura, *Nano Lett.* **2008**, *8*, 369.

[44] J. Zhang, X. Li, J. M. Rosenholm, H. chen Gu, *J. Colloid Interface Sci.* **2011**, *361*, 16.

[45] J. F. Li, X. D. Tian, S. B. Li, J. R. Anema, Z. L. Yang, Y. Ding, Y. F. Wu, Y. M. Zeng, Q. Z. Chen, B. Ren, Z. L. Wang, Z. Q. Tian, *Nat. Protoc.* **2013**, *8*, 52.

[46] J. E. S. van der Hoeven, J. Jelic, L. A. Olthof, G. Totarella, R. J. A. van Dijk-Moes, F. Studt, A. van Blaaderen, P. E. de Jongh, *Nat. Mater.* **2021**, *20*, 1216.

[47] B. De Nijs, S. Dussi, F. Smallenburg, J. D. Meeldijk, D. J. Groenendijk, L. Filion, A. Imhof, A. Van Blaaderen, M. Dijkstra, *Nat. Mater.* **2015**, *14*, 56.

[48] J. E. S. Van Der Hoeven, E. B. Van Der Wee, D. A. M. De Winter, M. Hermes, Y. Liu, J. Fokkema, M. Bransen, M. A. Van Huis, H. C. Gerritsen, P. E. De Jongh, A. Van Blaaderen, *Nanoscale* **2019**, *11*, 5304.

[49] K. L. Wustholz, A. I. Henry, J. M. McMahon, R. G. Freeman, N. Valley, M. E. Piotti, M. J. Natan, G. C. Schatz, R. P. V. Duyne, *J. Am. Chem. Soc.* **2010**, *132*, 10903.

[50] A. I. Henry, J. M. Bingham, E. Ringe, L. D. Marks, G. C. Schatz, R. P. Van Duyne, *J. Phys. Chem. C* **2011**, *115*, 9291.

[51] J. Wang, C. F. Mbah, T. Przybilla, B. Apeleo Zubiri, E. Spiecker, M. Engel, N. Vogel, *Nat. Commun.* **2018**, *9*, 5259.

[52] F. Montanarella, D. Urbonas, L. Chadwick, P. G. Moerman, P. J. Baesjou, R. F. Mahrt, A. Van Blaaderen, T. Stöferle, D. Vanmaekelbergh, *ACS Nano* **2018**, *12*, 12788.

[53] Z. Gao, N. D. Burrows, N. A. Valley, G. C. Schatz, C. J. Murphy, C. L. Haynes, *Analyst* **2016**, *141*, 5088.

[54] O. Chen, L. Riedemann, F. Etoc, H. Herrmann, M. Coppey, M. Barch, C. T. Farrar, J. Zhao, O. T. Bruns, H. Wei, P. Guo, J. Cui, R. Jensen, Y. Chen, D. K. Harris, J. M. Cordero, Z. Wang, A. Jasanoff, D. Fukumura, R. Reimer, M. Dahan, R. K. Jain, M. G. Bawendi, *Nat. Commun.* **2014**, *5*, 5093.

[55] T. H. Besseling, M. Hermes, A. Kuijk, B. De Nijs, T. S. Deng, M. Dijkstra, A. Imhof, A. Van Blaaderen, *J. Phys. Condens. Matter.* **2015**, *27*, 194109.

[56] G. Bodelón, V. Montes-García, V. López-Puente, E. H. Hill, C. Hamon, M. N. Sanz-Ortiz, S. Rodal-Cedeira, C. Costas, S. Celiksoy, I. Pérez-Juste, L. Scarabelli, A. La Porta, J. Pérez-Juste, I. Pastoriza-Santos, L. M. Liz-Marzán, *Nat. Mater.* **2016**, *15*, 1203.

[57] Y. Liu, M. Kim, S. H. Cho, Y. S. Jung, *Nano Today* **2021**, *37*, 101063.

[58] F. Montanarella, J. J. Geuchies, T. Dasgupta, P. T. Prins, C. Van Overbeek, R. Dattani, P. Baesjou, M. Dijkstra, A. V. Petukhov, A. Van Blaaderen, D. Vanmaekelbergh, *Nano Lett.* **2018**, *18*, 3675.

[59] B. N. Khlebtsov, V. A. Khanadeev, A. M. Burov, E. C. Le Ru, N. G. Khlebtsov, *J. Phys. Chem. C* **2020**, *124*, 10647.

[60] A. Samanta, S. Jana, R. K. Das, Y. T. Chang, *RSC Adv.* **2014**, *4*, 12415.

[61] H. Kang, C. Haynes, *J. Phys. Chem. C* **2019**, *123*, 24685.

[62] W. C. Wu, J. B. Tracy, *Chem. Mater.* **2015**, *27*, 2888.